A seismic network to monitor the 2020 EGS stimulation in the Espoo/Helsinki area, southern Finland

Rintamäki, Annukka Elina

2021-11-24

Rintamäki , A E , Hillers , G , Vuorinen , T , Luhta , T , Pownall , J , Tsarsitalidou , C , Galvin , K , Keskinen , J , Kortström , J , Lin , T-C , Mäntyniemi , P , Oinonen , K , Oksanen , T J , Seipäjärvi , P J , Taylor , G , Uski , M , Voutilainen , A I & Whipp , D 2021 , ' A seismic network to monitor the 2020 EGS stimulation in the Espoo/Helsinki area, southern Finland ' , þÿ S e i s m o l o g i c a l R e s e a r c h L e t t e r s , v o l . 9 3 , n o . 2 A , p p . 1 0 4 6 1 0 6 2 . h t t

http://hdl.handle.net/10138/351004
https://doi.org/10.1785/0220210195

unspecified
acceptedVersion

A seismic network to monitor the 2020 EGS stimulation in the Espoo/Helsinki area, southern Finland

Annukka E. Rintamäki[1], Gregor Hillers[1], Tommi A. T. Vuorinen[1], Tuija Luhta[1], Jonathan M. Pownall[1], Christina Tsarsitalidou[1], Keith Galvin[1,2], Jukka Keskinen[1], Jari T. Kortström[1], Tzu-Chi Lin[1], Päivi B. Mäntyniemi[1], Kati J. Oinonen[1], Tahvo J. Oksanen[1], Pirita J. Seipäjärvi[1], George Taylor[1,3], Marja R. Uski[1], Ahti I. Voutilainen[1,4], and David M. Whipp[1]

[1]Institute of Seismology, University of Helsinki, Pietari Kalmin katu 5, FI-00014 University of Helsinki, Finland
[2]Now at Terravision Exploration, 401 Walton Road, Molesey, Surrey, United Kingdom, KT8 2EG
[3]Now at Ocean Environment Team, United Kingdom Hydrographic Office, Taunton, United Kingdom, TA1 2DN
[4]Now at Boliden Minerals AB, Finnforsvägen 4, 93632 Boliden, Sweden

Corresponding author: Annukka Rintamäki, annukka.rintamaki@helsinki.fi

Abstract

We present the deployment of a seismic network in the Helsinki capital area of Finland that was installed to monitor the response to the second stimulation phase of a ∼6 km deep enhanced geothermal system in 2020. The network consists of a dozen permanent broadband stations and more than 100, predominantly short-period, temporary stations. This 2020 deployment is characterized by a mix of single stations and arrays with diverse configurations. It covers a larger area and exhibits a smaller azimuthal gap compared to the network that monitored the first stimulation in 2018. We surveyed the outcropping rocks at one of the large array sites to study surface expressions of shear or weakness zones that are possibly connected to the stimulated volume at depth. We link the relatively large number of macroseismic reports received during the stimulation to an increased public awareness of the project together with an increased sensitivity, since the second stimulation occurred during the local COVID-19 mobility restrictions. The spatial distribution of the reports seems to be controlled by the radiation pattern of the induced earthquakes and hence by the stress state in the reservoir. The continuous records contain strong energy at high frequencies above 50 Hz that is attributed to anthropogenic processes in the densely populated urban area. However, the exceptionally low attenuation of the bedrock yields good signal-to-noise ratio seismograms of the induced small events, the largest of which was magnitude $M_{\mathrm{L}}1.2$. The signal quality of the obtained noise correlation functions is similarly very good. The data set has been collected to underpin a wide range of seismic analysis techniques for complementary scientific studies of the evolving reservoir processes and the induced event properties. These scientific studies should inform the legislation and educate the public for transparent decision making around geothermal power generation.

Introduction

Tapping the heat of the Earth's crust using carbon-neutral geothermal systems has gained popularity as part of an array of strategies supporting the reduction of greenhouse gas emissions to mitigate global warming [e.g. *Majer et al.*, 2007; *Evans et al.*, 2012; *Laloui and Loria*, 2020]. Induced earthquakes are inextricably linked with the stimulation of an enhanced geothermal system (EGS) that seeks to facilitate an efficient heat exchange between circulating fluids and the rock [*Heuer et al.*, 1991]. The event sequences associated with stimulations in Basel, Switzerland [*Häring et al.*, 2008], Pohang, South Korea [*Ellsworth et al.*, 2019], and Strasbourg, France [*Schmittbuhl et al.*, 2021], resulted in earthquake ground motions that exceeded the limits considered to be acceptable, demonstrating the persistent challenges that have to be met before the EGS approach can be widely implemented.

Here we describe the data set collected with a seismic network in the Helsinki capital area of Finland in 2020 that recorded the response to a ∼6 km deep EGS stimulation below the Aalto University campus in the Otaniemi district of the City of Espoo (Fig. 1). This second stimulation from 6 May to 24 May 2020 established a geothermal doublet system. It enhanced the permeability between the second well and the fracture network created in the first larger 2018 stimulation [*Kwiatek et al.*, 2019] around the first well (Fig. 2). During the 2020 stimulation a total volume of 2,600 m^3 freshwater was pumped in several stages with maximum pumping pressures of 70 MPa. In 2020 the largest induced earthquake magnitude was $M_{\mathrm{L}}1.2$, hence in both 2018 and 2020 Otaniemi stimulations the magnitudes did not exceed the $M_{\mathrm{L}}2.1$ limit set by local authorities [*Ader et al.*, 2019]. After further tests planned for the second half of 2021 the system is anticipated to supply district heat.

These promising developments are understood to result from a combination of favorable geologic conditions and an adaptive stimulation protocol that included intermittent, quiet stages to allow the hydraulic energy to dissipate [*Galis et al.*, 2017; *Kwiatek et al.*, 2019]. The ∼6 km depth of the drill holes at the Otaniemi EGS site is necessitated by the cool, Precambrian bedrock of the Fennoscandian shield, but they may soon be superseded by 7 to 8 km deep holes planned in other municipalities in southern Finland. The geology in the shield area is characterized by exposed bedrock and the absence of younger sediments. It follows that attenuation is considerably low, and the signal-to-noise ratio (SNR) of even small-magnitude earthquake seismograms recorded at the surface is compelling [*Taylor et al.*, 2021]. Consequently, this EGS site situated in an intraplate cratonic, low-seismicity area constitutes an intriguing natural laboratory, and the collected data sets such as the one desribed here can help further our understanding of the stimulation response.

The Otaniemi 2020 network desribed here can be understood in the context of seismic monitoring systems that evolve along with the different stages of an EGS [*Majer et al.*, 2007; *Dorbath et al.*, 2009; *Evans et al.*, 2012; *Vasterling et al.*, 2017; *Kim et al.*, 2018]. The multi-component network (Fig. 1) consisted of permanent and temporary subnetworks, different sensor types and recorders, and a variable number of stations per site (Tables 1, 2). Data from the permanent satellite borehole stations operated in 2018 and 2020 by the St1 Deep Heat Company underpinned the real-time monitoring and the industrial catalog [*Kwiatek et al.*, 2019]. The resolved seismicity patterns continue to be a resource for reservoir stimulation response analyses [*Bentz et al.*, 2020; *Leonhardt et al.*, 2021].

Here we focus on the dozens of temporary short-period stations managed by the Institute of Seismology, University of Helsinki (ISUH), in the Helsinki, Espoo, and Vantaa area between November 2019 and July 2020. The 2020 deployment builds on experiences and results obtained during the 2018 stimulation phase [*Hillers et al.*, 2019, 2020]. Key components of the ISUH 2018 temporary network were three large and three small seismic arrays. The 2020 network also includes arrays, often in the same locations, but it additionally reduces azimuthal gaps and extends the network aperture compared to the 2018 deployment. Together with the stand-alone stations the 2018 records were used for seismicity analyses, initial passive imaging and monitoring studies [*Hillers et al.*, 2020], characterization of the local scattering length scales [*Wegler et al.*, 2020], displacement variation-based estimates of rotational ground motion [*Taylor et al.*, 2021], beamforming and backprojection approaches for earthquake property estimates [*Li et al.*, 2021], and for constraining ground motion prediction equations [*Voutilainen*, 2021].

The combined data sets enable further detailed analysis of the evolving reservoir characteristics [*Calò and Dorbath*, 2013; *Hillers et al.*, 2015; *Diehl et al.*, 2017; *Holtzman et al.*, 2018], induced earthquake properties [*Goertz-Allmann et al.*, 2011; *Martínez-Garzón et al.*, 2017], and triggering mechanisms [*Dahm et al.*, 2013; *Ellsworth et al.*, 2019]. The array data can help improve moment tensor estimates based on six degrees of freedom observations [*Donner et al.*, 2016; *Taylor et al.*, 2021]. A better discrimination of volumetric and shear components for small events is essential for connecting in-situ and laboratory physics [*Renard et al.*, 2019], for resolving posited damage waves [*Calò et al.*, 2011; *Shalev et al.*, 2013], and for the assessment of the reservoir permeability and fluid diffusion [*Terakawa et al.*, 2012]. More complete, direct observations of in-situ physical processes constrain the mechanisms that govern the earthquake size distribution [*McGarr*, 2014; *van der Elst et al.*, 2016; *Galis et al.*, 2017; *Lyakhovsky and Shalev*, 2021], and calibrate poro-elastic models for evolving properties of rocks undergoing irreversible brittle deformation [*Shalev and Lyakhovsky*, 2018]. Comparison of catalogs obtained with borehole and surface station data can guide investements in the network infrastructure for future deployments in similar geological conditions. The insigths gained from this study will contribute to designing stimulation protocols and monitoring systems, and inform legislators in the safe implementation and improved public acceptance of geothermal power generation.

Experiment design

To cover the 2020 stimulation ISUH established a diverse seismic network that combined permanent, semipermanent, and temporary stations around the Otaniemi stimulation site. The backbone is formed by 11 ISUH permanent stations that were complemented by 116 temporary instruments. This note describes primarily this temporary network (red, yellow, and light-blue stations in Figs. 1, 2). The evolution from the 2018 network to the 2020 network—that is split into three subnetworks HE, OT, OX (Table 1, Fig. 3)—is essential, and we describe key relations between parts of these two ISUH networks to facilitate a combined analysis. The ISUH networks complement the 12 permanent satellite borehole stations (gray circles in the main map in Fig. 1) [*Kwiatek et al.*, 2019] operated by St1. Their power supply was updated in 2019 to be independent of solar energy and to improve network reliability during the winter months. Data from these stations have been transmitted to ISUH but are not released to the public and are hence not further discussed here.

Permanent stations

Stations operated by ISUH include the three Finnish National Seismic Network (FNSN) broadband stations MEF, NUR, PVF (black circles in Fig. 1) [*Veikkolainen et al.*, 2021a], five broadband stations HEL1 to HEL5 deployed in 2016 and 2017 to monitor the seismicity associated with the reservoir development, and three new broadband stations KUNI, LAUT, VUOS (dark blue circles in Fig. 1) of the HelsinkiNet that were commissioned in 2019 and 2020 by the City of Helsinki for monitoring purposes. These permanent broadband stations are together referred to as the HE subnetwork in Table 1 and in Figure 3. They are powered by the electric grid and data transmission is continuous [*Veikkolainen et al.*, 2021a].

Temporary stations

The 113 temporary geophones and 3 temporary short-period seismometers were installed as 6 stand-alone stations and 19 arrays of 3 to 17 stations. The 2020 temporary network data were archived as two subnetworks OT and OX (Table 1, Fig. 3). Key changes compared to the 2018 deployment include the network aperture increase, reducing the azimuthal gap in the Gulf of Finland to the south by installing two island arrays, and increasing the number of small 3-station arrays while decreasing the number of stations at large arrays from 25 to 7. In 2018, the majority of 100 temporary instruments were installed within $\sim$6 km of the stimulation site, but in 2020 we aimed at distributing them more homogeneously within a $\sim$23 km radius. When all network stations are considered, the azimuthal gap narrowed from $38°$ in 2018 to $31°$ in 2020, and when stations at distances of 5 km or larger around the stimulation site are considered, the gap decreased from $140°$ to $56°$.

The larger network area can help to better discriminate natural from induced or triggered events. Although this may seem to have little relevance in this low-seismicity environment, the occurrence of small-magnitude earthquakes in November and December 2020 in Koskelo, Espoo, in the vicinity of the Porkkala-Mäntsälä fault 10 km to the northwest of the EGS site [*Veikkolainen et al.*, 2021b], within a few hundred meters of a 1.3 km deep thermal well, does emphasize the advantage of denser over sparser seismic monitoring systems.

In 2020 we deployed 70 pairs of 4.5 Hz three-component geophones and DATA-CUBE3 recorders (hereafter referred as cubes or cube stations) from the Geophysical Instrument Pool Potsdam (GIPP) that sampled at 400 Hz. These stations form the OT subnetwork. In 2018, all 100 temporary stations were GIPP cubes. Then as now they relied on built-in Global Positioning System (GPS) receivers, and have 16 or 32 GB Secure Digital High Capacity (SDHC) cards for data storage that were downloaded and cleared in regular intervals [*Hillers et al.*, 2020]. In 2020 the cube stations were arranged as 3 stand-alone stations and 16 arrays as detailed in Section Arrays (Tables 1, 2; red symbols in Figs. 1, 2). To simplify the maintenance of the numerous instruments across a large area we used an improved battery solution compared to packs of 8 D-cells that were used for all cubes in 2018. We chose 9 V, 150 Ah air-alkaline batteries (fence batteries) to power the majority of the temporary network stations, and only a few stations at easy-to-access locations were powered by the 8 D-cell packs that required battery changes approximately every 30 days. The fence batteries possessed an extended lifespan of just over four months, meaning that batteries had to be changed only at those few stations that started operation in 2019 (Fig. 3). Excess humidity or submergence during wet periods was responsible for some power failures, which could also be caused by insufficient air flow to the battery. We mitigated these challenges by water-tight packaging and ensuring adequate air flow to the device with tubing that had a sufficiently large diameter of 3 cm (Fig. 4a, b).

In 2020 we deployed 44 5 Hz three-component SmartSolo instruments with internal GPS and 118 GB memory owned by ISUH (yellow symbols in Figs. 1, 2). The 34 instruments that were arranged in two 17-station arrays relied on internal batteries and sampled at 500 Hz. Four sensors deployed on the Koirasaari island (KS array in Fig. 1) and six on Lauttasaari (AS array) were equipped with the fence batteries to extend the recording period.

The last three temporary stations were ISUH-owned pairs of 1 Hz Lennartz LE-3Dlite sensors coupled with REF TEK recorders (light blue circle in Figs. 1, 2; hereafter referred to as Refteks) sampling at 500 Hz except for the ZAK50 station, which sampled at 250 Hz for the first 13 days. They used external GPS and two fence batteries connected in series. Here, a shorter-than-expected battery life resulted in recording gaps. The SmartSolo and Reftek stations data were archived as OX subnetwork (Table 1, Fig. 3).

Timing

The deployment began on 28 November 2019 and ended on 14 July 2020. The deployment times and locations of the temporary stations are collected in Table 2. The second stimulation was originally scheduled to start in January 2020, but it was several times delayed until it commenced in May 2020. This delay caused the sparse installation between December 2019 and February 2020 and it necessitated the prolongation of the temporary deployment. During the winter the average temperature in southern Finland remained a few degrees above 0°C, which is significantly warmer than the long-term average. Consequently, the batteries lasted much longer than anticipated, the ground was easy to dig throughout the experiment, and no snow cover hid the stations. Overall, the mild winter combined with the delay of the stimulation facilitated the deployment management—but the COVID-19 related restrictions clearly complicated it.

We began to deploy the network in late 2019, and the number of installed stations increased until early March 2020 when a large part of the network was complete. Few stations continued to be added until 6 May 2020, when the two arrays of 17 SmartSolos were installed to record the response to the imminent stimulation. These two arrays were in operation for two weeks until the internal batteries were exhausted. The KS array was removed on 10 June

2020, and the SL array was removed on 1 July 2020. Most of the temporary stations were operating until mid-July 2020. The resulting data availability (Fig. 3) is revisited in Section Overall data quality and availability.

Locations and installation

Temporary network stations were installed at easily accessible bedrock outcrop sites that together establish good azimuthal coverage in a diverse distance range around the Otaniemi EGS. Our experience with several station and array locations in 2018 facilitated the design and selection process. New sites were established for the network expansion on shore and on islands. To reduce the azimuthal gap to the south of the study area, two small arrays were installed on islands off the coast of Helsinki. The OT three-station SL array was installed inside a prison domain on Suomenlinna islands. The second KS array consisting of three cubes and four SmartSolos was installed on Koirasaari island. This deployment relied on the support from the City of Helsinki for boat transfer. Most stations were installed in public areas such as forests and meadows. No permitting issues interfered, as allowed by the *jokamiehenoikeus* principle or everyman's right, a legal concept in Finland and other Nordic countries that allows free access to the environment as long as exercised activities do not cause visible or lasting changes.

A few instruments were dug up by passersby in popular recreational areas, and one instrument went missing from the MN array so that data were recovered from 16 of the originally 17 stations. Cubes and SmartSolos were installed by digging a 20 to 50 cm deep hole, and coupling the sensor to the prevailing sedimentary material. Sand from a hardware store was used for improved coupling in areas where only a thin topsoil or peat layer covered the bedrock (Fig. 4). Recorders and batteries were buried in plastic bags and covered with organic matter to blend the instruments into the landscape while allowing GPS signal transmission.

Two museums and a hotel continued the cooperation from the 2018 campaign and we deployed the Refteks on their access-limited properties. We placed the Lennartz sensor on flat bedrock outcrop, and stored the recorder and battery in a plastic box.

A handheld Brunton compass that was corrected for magnetic declination was used for sensor orientation. A handheld Garmin GPSMAP 66st GPS device was used to record station location. Station elevations were estimated retrospectively from an elevation model with 2 m resolution from the National Land Survey of Finland using the GPS locations.

Station codes are made up of two or three letters that refer to the installation location followed by a number starting from 50 to make the stations easy to identify from the stations of the 2018 deployment (Table 1, Fig. 3). In rare cases stations were relocated before the stimulation if the initial location became unsuitable because it was flooded or if the instruments had repeatedly been found by passersby. Figures 1 and 2 show the final locations of the stations that were recording during the stimulation.

Data downloads were scheduled at 30−35 day intervals for cubes with 16 GB SDHC cards and at 50−60 day intervals for cubes with 32 GB cards. The interval between Reftek installation and the first maintenance visits was in retrospect with 36 days too long for the 20 days the batteries powered the stations. The COVID-19 related restrictions limited the possibilities for prior testing or more frequent maintenance visits. SmartSolos did not require maintenance breaks during the deployment but visits were made to confirm their working order.

Arrays

The short-period cube stations and SmartSolo instruments were installed in arrays consisting of 3 to 17 instruments. The array aperture of the larger arrays varied between 100 m and 180 m. The interstation distance was typically in the 50 m range at all arrays. These length scales facilitate the application of array techniques [*Hillers et al.*, 2020; *Li et al.*, 2021; *Taylor et al.*, 2021] to the low-frequency parts of the earthquake seismograms in the 1−10 Hz range.

Three larger cube arrays SS, EV, and TL were located within a 5.2 km radius from the injection site. These 2020 locations were the same as in the 2018 deployment, except the TL array site was moved 350 m to the west to a stable rock outcrop. The corresponding 2018 arrays consisted of nominally 25 stations, but in 2020 the SS and TL arrays had 7 stations and the EV array had 11 stations. Each had 7 stations in a hexagonal geometry, and the EV array was extended by a line array crossing the hexagon (Figs. 1, 2). The aperture of the hexagonal arrays were ∼95 m at the TL site, ∼135 m at SS, and ∼145 m at EV. The EV line array was ∼420 m long.

Three four-station cube arrays were installed within 6.3 km around the borehole. The PM and PK arrays occupied the same sites as in 2018, and the EK array replaced the 2018 RS array at a site 1.1 km to the north-west that is not landscaped and therefore anticipated to yield better data quality [*Taylor et al.*, 2021]. Nine tripod arrays with three instruments were installed at distances between 7 and 23 km from the injection site. On the Koirasaari island 11.5 km to the south of the borehole the tenth three-cube KS array was augmented by four

SmartSolo sensors for redundancy since no maintenance trips could be reliably planned in advance, and to allow for the opportunity to enhance the signal quality from this environmentally exposed location through stacking. The other SmartSolo devices were deployed in two 180 m aperture, 17-sensor SH and MN arrays at 4.8 km and 2.7 km west and north-east, respectively, of the injection site, configured in three circles of three, five, and eight sensors around a central station. One sensor at MN was permanently lost.

Similar to the reused sites, the new 2020 cube array sites were also characterized by outcropping bedrock with a thick enough—though sometimes still only a few centimeters thick—layer of organic material to facilitate installation. In contrast, the SmartSolo 17-station SH and MN arrays were deployed on a fallow agricultural field and in an open park area. The sites were chosen on very short notice (Fig. 3) and the two arrays deployed within seven hours, hence convenience—accessibility, maneuverability, and visibility—trumped bedrock coupling.

The larger arrays consisting of 7 and 17 sensors at close range were deployed to collect data for array-processing techniques [*Hillers et al.*, 2020; *Li et al.*, 2021; *Taylor et al.*, 2021]. The array response functions in the lower row of Figure 5 indicate that the increased apertures of the SS, EV, and TL arrays enhance the resolution compared to the corresponding 2018 arrays shown in the upper row. Considering the known hypocentral area the spatial aliasing resulting from the fewer stations organized in a hexagonal geometry does not play a role. The localized SH and MN response functions can support earthquake source studies by providing well-constrained estimates of the local wave propagation. The idea behind the tripod array deployment was to enlarge the temporary network and to increase the signal-to-noise ratio by stacking seismograms of the small-magnitude events for improved moment tensor solutions.

Geological structures at Elfvik

Here we describe the results of a geological survey of the outcropping rocks at the Elfvik array site. We were interested in surface expressions of shear or weak zones, and in the possible connection to the deep reservoir that can be probed with the array records of induced events.

A steeply southward-dipping subsurface structure 1 to 2 km north of the EGS site was suggested to intersect the geothermal wells and the stimulated volume at 5 to 6 km depth [*Kwiatek et al.*, 2019]. This description fits an E-W trending structure [*Elminen et al.*, 2008; *Pajunen et al.*, 2008] parallel to and intersecting the E-W running Highway 1 and its intersection with the N-S running Ring 1 trunk road, which prohibited a detailed assessment (Fig. 2). However, the description also fits ENE-WSW trending weakness zones in Elfvik [*Pajunen et al.*, 2008]

$\sim$500 m closer towards the stimulation site (Figs. 2, 6). These zones have been related to Proterozoic NE-SW trending near-vertical ductile shear zones [*Elminen et al.*, 2008].

To investigate possible seismic wave interaction with and around the Elfvik weakness zones and their relation to the stimulated volume, we complemented the 2D EV array by a line array and mapped the geological structures in the area in June 2020. We identified several parallel ENE-WSW trending subvertical shear bands (Fig. 6). These approximately planar shear zones are close to vertical, dipping at least 80° either northwards or southwards. These clearly identified features are not, however, compatible with the local weakness zone reported by *Pajunen et al.* [2008], that is approximated by the gray dashed line in Figure 6 some 100 m to the south. This zone coincides at best with the N-S gradient in the topography. Taken together, it is not clear whether the observed shear structures are part of a weakness zone that extends downwards towards the south such that it intersects the geothermal wells at reservoir depth.

However, our survey across the EV array site facilitates the interpretation of seismic data in a context of detailed geological observations. Investigations including high-frequency polarization analysis [*Jepsen and Kennett*, 1990], 2D passive imaging along the line array [*Hillers and Campillo*, 2018], or analyses targeting waves refracting along material contrasts [*Ben-Zion et al.*, 1992; *Lin et al.*, 2020] can help clarify whether the observed N-S gradients in event signal quality [*Hillers et al.*, 2020] or displacement gradients [*Taylor et al.*, 2021] are governed by near-surface properties or controlled by deeper structure.

Overall data quality and availability

The different instrument response functions are displayed in Figures 7a and e. Signals collected with these sensor types are of good quality at frequencies greater than 0.1 Hz. As detailed below, the various sensors yield on average high-SNR records of regional and local earthquake waveforms, and well resolved surface wave signals are obtained from cross-correlation of ambient seismic field records. The vertical component noise anatomy from 100 days of data including the stimulation period in the 0.1−100 Hz range shows that the 4.5 Hz cube stations (Figs. 7b−d, f−h) resolve seismic noise in the range of the secondary microseisms, although the sensitivity at these low frequencies is limited compared to the broadband stations (Figs. 7a, e, h). Noise amplitude distributions show a minimum around 2 Hz but distinctively elevated energies towards higher frequencies.

Stations located in coastal, rural, and urban settings record maximum energy levels in the 60−80 Hz range (TL, PO, EV; Figs. 7b−d). Energy in this range is still elevated, comparable to the secondary microseisms, but less peaked at remote inland stations (SV; Fig. 7f) and in a dense forest environment close to human activity (EK; Fig. 7g). These observations from diverse settings suggest high-frequency energy is related to site-specific contributions from environmental processes, mostly wind, and anthropogenic activity [*Hillers et al.*, 2020], including the induced earthquakes, traffic, and explosions associated with numerous construction activities. We highlight the elevated amplitudes between 0.5 and 80 Hz at the broadband HEL3 station (Fig. 7h) within 100 m of a trunk road and an underground railway. Interestingly, the Helsinki noise level reduction associated with the 2020 lockdown to curb the transmission of the COVID-19 virus was only observed in the 60−90 Hz range, in contrast to the global observations reported in the 4−14 Hz range [*Lecocq et al.*, 2020]. This, too, suggests that a significant component of the high-frequency wavefield is excited and modulated by anthropogenic activity patterns. The noise level does not, however, obfuscate the induced event signals. Comparing the spectral amplitude of two seconds long induced event seismograms recorded at the surface to pre-P wave noise yields overall high SNRs that are, as said, modulated by anthropogenic patterns, up to the Nyquist frequency. Pending studies focus on the detection capability and spectral power as a function of earthquake depth, location, and magnitude, the number of sensors per site, and the ambient noise level to inform future network infrastructure in similar geological conditions.

Figure 3 indicates that the overwhelming majority of the stations were operational during the stimulation in May 2020. Continuous lines before and after the stimulation stage and the high percentages indicate a high return rate of the invested resources. Short data segments from the OT stations LS53, PM54, PM55, SS57, SS58, and SS59 (Fig. 3a) that do not cover the stimulation are associated with problems of the original installation. The stations were removed and installed at another site with a new station code. The defining feature of the OX subnetwork SmartSolo arrays MN and SH is the 12-hour on/off cycling that was chosen to extend the battery life (Fig. 3b). The intermittent data availability at the HAN50, WEG50, and ZAK50 Reftek stations is governed by the above mentioned power supply problems (Fig. 3c). Last, the permanent HE stations from the HEL, HelsinkiNet, and FNSN networks (Fig. 3d) also show a good coverage for the period of the 2020 OT cube deployment. The repositories and data centers where the data can be accessed are described in the Data and Resources section.

Initial observations and results

Induced seismicity and macroseismicity

Seismic events were detected using online station data from the HE network (Table 1) and St1 borehole stations (Fig. 1). The short-term average over long-term average algorithm parameters are described in *Hillers et al.* [2020]. Automatically picked P wave and S wave arrivals are manually refined by ISUH analysts. Between January and September 2020 our system detected 83 induced earthquakes (black data in Fig. 2, Fig. 3e) in close proximity to the second borehole [*Veikkolainen et al.*, 2020]. We used the Finnish local magnitude scale M_{L} [*Uski and Tuppurainen*, 1996] as for the 2018 stimulation analysis [*Hillers et al.*, 2020]. The earthquake locations are computed from the revised arrival times using a standard linear least-squares algorithm and the velocity model from *Kortström et al.* [2018].

The seismicity time line in Figure 3e shows events before and after the stimulation phase. Drilling of the OTN2 well began 21 September 2019 and was completed on 8 March 2020. Drilling, cleaning, and logging operations could explain the pre-stimulation events. Decreasing seismicity after the stimulation is frequently observed and typically associated with stress equilibration processes. The two largest induced $M_{\mathrm{L}}1.2$ events occurred before the stimulation on 14 April 2020 and during the stimulation on 17 May 2020 at a depth of 5.5 km and within 160 m distance to each other [*Veikkolainen et al.*, 2020]. Source mechanisms estimated with FOCMEC [*Snoke*, 2003] based on online station data (Fig. 2) show almost identical oblique mechanisms with strike-slip and thrust components [*Veikkolainen et al.*, 2020]. The high similarity to the prevailing focal mechanisms of the events induced by the 2018 stimulation [*Hillers et al.*, 2020; *Leonhardt et al.*, 2021], and the close proximity of the two seismicity distributions imply an overall similar governing stress regime.

In April and May 2020 ISUH received in total 111 macroseismic observations associated with 17 induced earthquakes in the $M_{\mathrm{L}}-0.8$ to 1.2 range (Fig. 8). In 2018 ISUH collected 220 responses, but it was not possible to determine the number of earthquakes or the magnitude range that these responses were associated with, because many reports summarised several obserservations of ground motions over some weeks [*Hillers et al.*, 2020]. It is likely that the relatively high number of macroseismic reports during the smaller 2020 stimulation is related to an increased public awareness of the project and of the induced seismicity [*Veikkolainen et al.*, 2021b]. An increased awareness seems to meet an increased sensitivity during the COVID-19 related low-mobility period from March to May 2020 experienced by a significant number of residents.

Radiation patterns of the two largest induced events (Fig. 8b) show the absolute values of the theoretical radiation factors for SH, SV, and P waves at the surface accounting for geometrical spreading. Similar to the observations in 2018, Figure 8(b) implies that the macroseismic response distribution is controlled by the combined SH and SV wave radiation emanated from the oblique faults, and hence by the rupture geometry and ultimately by the stress state in the hypocentral region. The similarity extends to reports of various combinations of shaking and sound sensations. This implies, again, that weakly attenuated high-frequency seismic-wave energy excites audible infrasound propagation [*Lamb et al.*, 2021]. These consistent reports suggest that the impact of EGS stimulations in densely populated areas in similar geologic environments not only includes ground shaking and vibration phenomena but also sound propagation, which may be considered in the permitting process.

Regional earthquake waveforms

Example waveforms demonstrate the high quality of the collected seismic records. Our network recorded waves excited by the 18 May 2020 mine collapse event with moment magnitude $M_{\mathrm{w}}4.1$ that occurred on 01:11:56 UTC at the Kiruna iron ore mine in northern Sweden (67.834°N, 20.216°E). Figure 9(a) shows the first arriving P waves recorded by the available OT, OX, HEL, and HelsinkiNet stations. Cube and SmartSolo station records are stacked per array. The instrument response has not been removed for this illustration. The clean onsets and high signal-to-noise ratio of the P waves in the $0.5-2.5$ Hz range that propagated almost 1000 km at an average speed of 7.8 km/s through the Fennoscandian shield highlight the low wave attenuation of the cratonic material on these regional scales. Such signals can be used to assess the timing and orientation of the deployed instruments and to verify the integrity of the data. On the scale of individual arrays, waveform similarity as shown in Figure 9(b) can help to identify problematic installation and coupling effects.

Local induced event

Figure 9(c) shows $1-10$ Hz vertical component velocity seismograms of a $M_{\mathrm{L}}1.2$ event that occurred on 17 May 2020 at 00:06:30 local time in 5.6 km depth. From its location (Fig. 2) and timing (Fig. 3) it is understood that the earthquake was induced. Records from the TL array south-west of the stimulated volume shown in Figure 9(d) exhibit clean P wave and S wave arrivals that can be analyzed using various single station and array processing techniques to study source properties and propagation effects.

Noise correlations

Surface waves in ambient noise correlations exhibit good signal quality. Figure 10 shows results using data from 130 days recorded by the cube arrays. Processing is identical to *Hillers et al.* [2020]. The 400 Hz records are split in 1 hr segments, whitened between 0.2−20 Hz, amplitude-clipped at three times the standard deviation of the amplitude distribution in each processing window, filtered, tapered, downsampled to 50 Hz, cross-correlated, and stacked after a correlation amplitude-based quality check. The full stacks are rotated from the ZNE to the ZRT system. The shown seismograms are averages of the 3×3 to 7×11 station pairs between the cube arrays. We limit the illustration to a subset of the 120 possible array pairs for clarity. The waveforms filtered in the 0.25−1 Hz (Fig. 10a) and 1−4 Hz range (Fig. 10b) exhibit high-SNR Rayleigh and Love wave signals. Dispersion in this frequency range around average speeds of 3 km/s is small, which reflects the high-velocity competent bedrock geology in southern Finland [*Hillers et al.*, 2020; *Tiira et al.*, 2020].

The good signal quality across distances of 40 km associated with the PO and IL array sites in the southwest and northeast (Fig. 1) extends the Rayleigh wave depth resolution in the study area down to 4−5 km compared to the 2018 network that had a smaller aperture. The target passive surface wave tomography including data from the two deployments does still not fully resolve the reservoir depth. However, a combined inversion with body wave arrival data [*Fang et al.*, 2016, 2018] from the induced earthquakes has the potential to image the volume above and including the reservoir, and to facilitate the comparison with independently obtained velocity models from vertical seismic profiling [*Kwiatek et al.*, 2019; *Leonhardt et al.*, 2021].

Summary

We discussed properties of a seismic network that was deployed to monitor the second stimulation of a more than 6 km deep geothermal system in 2020 in the Helsinki area, southern Finland. More than 100 seismic stations were temporarily deployed to maximize the scientific return of this in-situ experiment. The good signal-to-noise ratio of the recorded small-magnitude induced earthquakes is exemplary of the high quality of the collected data set, which can be attributed to the low attenuation rock units in the cratonic study area. Together with the data collected around the first stimulation in 2018, the seismic records obtained with a mix of single stations and arrays can underpin a diverse range of seismic analysis techniques, that together will facilitate a comprehensive and complementary characterization of the stimulation responses. A more complete assessment of source, propagation, and site effects will not only increase the scientific impact of this pilot project, but it can also support the evolving legislation and decision making process, and it can facilitate the education of a public that has very limited exposure to natural seismic phenomena [*Mäntyniemi et al.*, 2017].

Data and resources

Seismograms from the Finnish National Seismic Network (FNSN) can be retrieved through the GEOFON Program hosted by the GFZ German Research Centre for Geosciences. Data from the other broadband HE monitoring stations (HEL1−HEL5, KUNI, LAUT, VUOS) and the OX Reftek stations are available through the Institute of Seismology, University of Helsinki. The 70 OT short-period sensors and the DATA-CUBE3 loggers were provided by the Geophysical Instrument Pool Potsdam (GIPP) under the Grant 201925-ORS2. The standard GIPP moratorium period applies. The data (1.6 TB) can be accessed after 31 August 2024 from the GIPP repository [*Hillers et al.*, 2021a]. Metadata is available through the same repositories. Technical information and software for translating the proprietary data format into MSEED are provided by the GIPP through its webpages. The OX SmartSolo data (0.5 TB) can be retrieved from the IDA Research Data Storage Service offered by the Finnish CSC IT Center for Science [*Hillers et al.*, 2021b]. Data from the 12 St1 borehole sensors have been transmitted to the Institute of Seismology at the University of Helsinki (ISUH) as part of a regulatory agreement with the City of Espoo. They are not released to the public. We used Pyrocko [*Heimann et al.*, 2017] for the cube data conversion. Parts of the analysis were implemented using ObsPy [*Krischer et al.*, 2015]. OpenStreetMap and the Generic Mapping Tools [*Wessel et al.*, 2013] were used to create the spatial displays.

Declaration of Competing Interests

The authors acknowledge there are no conflicts of interest recorded.

Acknowledgments

The authors thank Christian Haberland and the GIPP management for their support and assistance. The ISUH team thanks the City of Helsinki, Suomenlinna prison, Hanaholmen Cultural Centre, Hotel Hilton Kalastajatorppa, Gallen-Kallela Museum, Exhibition Centre Weegee, Didrichsen Art Museum, Poliisien kesäkoti Lauttasaari, Solvalla Sports Institute, and the Central Union of Agricultural Producers and Forest Owners (MTK) for supporting the deployment by providing access to installation sites. We appreciate the information on the drilling time line provided by St1. We thank A. Korja for an in-house review and two anonymous reviewers for comments that helped to improve the manuscript. A. Rintamäki is funded by the K.H. Renlund foundation. This research was supported by the Academy of Finland (decision no. 337913).

References

Ader, T., M. Chendorain, M. Free, T. Saarno, P. Heikkinen, P. E. Malin, P. Leary, G. Kwiatek, G. Dresen, F. Bluemle, and T. Vuorinen (2019), Design and implementation of a traffic light system for deep geothermal well stimulation in Finland, *Journal of Seismology*, *24*, 991–24, doi:10.1007/s10950-019-09853-y.

Ben-Zion, Y., S. Katz, and P. Leary (1992), Joint inversion of fault zone head waves and direct P arrivals for crustal structure near major faults, *Journal of Geophysical Research*, *97*, 1943–1951, doi:10.1029/91JB02748.

Bentz, S., G. Kwiatek, P. Martínez-Garzón, M. Bohnhoff, and G. Dresen (2020), Seismic Moment Evolution During Hydraulic Stimulations, *Geophysical Research Letters*, *47*, e2019GL086185, doi:10.1029/2019GL086185.

Calò, M., and C. Dorbath (2013), Different behaviours of the seismic velocity field at Soultz-sous-Forêts revealed by 4-D seismic tomography: case study of GPK3 and GPK2 injection tests, *Geophysical Journal International*, *194*, 1119–1137, doi: 10.1093/gji/ggt153.

Calò, M., C. Dorbath, F. H. Cornet, and N. Cuenot (2011), Large-scale aseismic motion identified through 4-D P-wave tomography, *Geophysical Journal International*, *186*, 1295–1314, doi:10.1111/j.1365-246X.2011.05108.x.

Dahm, T., D. Becker, M. Bischoff, S. Cesca, B. Dost, R. Fritschen, S. Hainzl, C. D. Klose, D. Kühn, S. Lasocki, T. Meier, M. Ohrnberger, E. Rivalta, U. Wegler, and S. Husen (2013), Recommendation for the discrimination of human-related and natural seismicity, *Journal of Seismology*, *17*, 197–202, doi:10.1007/s10950-012-9295-6.

Diehl, T., T. Kraft, E. Kissling, and S. Wiemer (2017), The induced earthquake sequence related to the St. Gallen deep geothermal project (Switzerland): Fault reactivation and fluid interactions imaged by microseismicity, *Journal of Geophysical Research: Solid Earth*, *122*, 7272–7290, doi:10.1002/2017JB014473.

Donner, S., M. Bernauer, and H. Igel (2016), Inversion for seismic moment tensors combining translational and rotational ground motions, *Geophysical Journal International*, *207*, 562–570, doi:10.1093/gji/ggw298.

Dorbath, L., N. Cuenot, A. Genter, and M. Frogneux (2009), Seismic response of the fractured and faulted granite of Soultz-sous-Forêts (France) to 5 km deep massive water injections, *Geophysical Journal International*, *177*, 653–675, doi:10.1111/j.1365-246X.2009.04030.x.

Ellsworth, W. L., D. Giardini, J. Townend, S. Ge, and T. Shimamoto (2019), Triggering of the Pohang, Korea, Earthquake (M_w 5.5) by Enhanced Geothermal System Stimulation, *Seismological Research Letters*, *90*, 1844–1858, doi:10.1785/0220190102.

Elminen, T., M.-L. Airo, R. Niemelä, M. Pajunen, M. Vaarma, P. Wasenius, and M. Wennerström (2008), Fault structures in the Helsinki area, southern Finland, *Special Paper - Geological Survey of Finland*, *47*, 185–213.

Evans, K. F., A. Zappone, T. Kraft, N. Deichmann, and F. Moia (2012), A survey of the induced seismic responses to fluid injection in geothermal and CO_2 reservoirs in Europe, *Geothermics*, *41*, 30–54, doi:10.1016/j.geothermics.2011.08.002.

Fang, H., H. Zhang, H. Yao, A. Allam, D. Zigone, Y. Ben-Zion, C. Thurber, and R. D. van der Hilst (2016), A new algorithm for three-dimensional joint inversion of body wave and surface wave data and its application to the Southern California plate boundary region, *Journal of Geophysical Research: Solid Earth*, *121*, 3557–3569, doi:10.1002/2015JB012702.

Fang, H., H. Yao, H. Zhang, C. Thurber, Y. Ben-Zion, and R. D. van der Hilst (2018), V_p/V_s tomography in the southern California plate boundary region using body and surface wave travelt ime data, *Geophysical Journal International*, *216*, 609–620, doi:10.1093/gji/ggy458.

Galis, M., J. P. Ampuero, P. M. Mai, and F. Cappa (2017), Induced seismicity provides insight into why earthquake ruptures stop, *Science Advances*, *3*, eaap7528, doi:10.1126/sciadv.aap7528.

Goertz-Allmann, B. P., A. Goertz, and S. Wiemer (2011), Stress drop variations of induced earthquakes at the Basel geothermal site, *Geophysical Research Letters*, *38*, L09308, doi:10.1029/2011GL047498.

Häring, M. O., U. Schanz, F. Ladner, and B. C. Dyer (2008), Characterisation of the Basel 1 enhanced geothermal system, *Geothermics*, *37*, 469–495, doi:10.1016/j.geothermics.

2008.06.002.

Heimann, S., M. Kriegerowski, M. Isken, S. Cesca, S. Daout, F. Grigoli, C. Juretzek, T. Megies, N. Nooshiri, A. Steinberg, H. Sudhaus, H. Vasyura-Bathke, T. Willey, and T. Dahm (2017), *Pyrocko - An open-source seismology toolbox and library*, GFZ Data Services, doi:10.5880/GFZ.2.1.2017.001.

Heuer, N., T. Küpper, and D. Windelberg (1991), Mathematical model of a Hot Dry Rock system, *Geophysical Journal International*, *105*, 659–664, doi:10.1111/j.1365-246X.1991.tb00803.x.

Hillers, G., and M. Campillo (2018), Fault zone imaging from correlations of aftershock waveforms, *Pure and Applied Geophysics*, *175*, 2643–2667, doi:10.1007/s00024-018-1836-7.

Hillers, G., S. Husen, A. Obermann, T. Planès, E. Larose, and M. Campillo (2015), Noise-based monitoring and imaging of aseismic transient deformation induced by the 2006 Basel reservoir stimulation, *Geophysics*, *80*(4), 51–68, doi:10.1190/GEO2014-0455.1.

Hillers, G., T. A. T. Vuorinen, E. J. Arola, V. E. Katajisto, M. P. Koskenniemi, B. M. McKevitt, S. Rezaei, L. A. Rinne, I. E. Salmenperä, P. J. Seipäjärvi, L. S. O. Väkevä, A. I. Voutilainen, K. Arhe, A. K. Juntunen, J. Keskinen, P. Y. Lindblom, K. Oinonen, and T. Tiira (2019), A 100 3-component sensor deployment to monitor the 2018 EGS stimulation in Espoo/Helsinki, southern Finland - Datasets, GFZ Data Services, doi:10.5880/GIPP.201802.1.

Hillers, G., T. A. T. Vuorinen, M. R. Uski, J. T. Kortström, P. B. Mäntyniemi, T. Tiira, P. E. Malin, and T. Saarno (2020), The 2018 Geothermal Reservoir Stimulation in Espoo/Helsinki, Southern Finland: Seismic Network Anatomy and Data Features, *Seismological Research Letters*, *91*, 770–786, doi:10.1785/0220190253.

Hillers, G., A. E. Rintamäki, T. A. T. Vuorinen, T. Luhta, K. Arhe, K. Galvin, J. Keskinen, J. T. Kortström, T.-C. Lin, P. Y. Lindblom, T. J. Oksanen, J. M. Pownall, P. J. Seipäjärvi, G. Taylor, C. Tsarsitalidou, A. I. Voutilainen, and D. M. Whipp (2021a), A 70 3-component sensor deployment to monitor the 2020 EGS stimulation in Espoo/Helsinki, southern Finland - Datasets, GFZ Data Services, doi:10.5880/GIPP.201925.1.

Hillers, G., A. Rintamäki, T. Vuorinen, T. Luhta, K. Arhe, K. Galvin, J. Keskinen, J. Kortström, T.-C. Lin, P. Lindblom, T. Oksanen, J. Pownall, P. Seipäjärvi, G. Taylor, C. Tsarsitalidou, A. Voutilainen, and D. Whipp (2021b), A temporary array deployment of

SmartSolo seismic sensors to monitor the 2020 EGS stimulation in Espoo/Helsinki, southern Finland (Version 1), doi:10.23729/ee530ff5-a5cf-4c09-bb81-cba793d4d08b.

Holtzman, B. K., A. Paté, J. Paisley, F. Waldhauser, and D. Repetto (2018), Machine learning reveals cyclic changes in seismic source spectra in Geysers geothermal field, *Science Advances*, *4*, doi:eaao2929.

Jepsen, D. C., and B. L. N. Kennett (1990), Three-component analysis of regional seismograms, *Bulletin of the Seismological Society of America*, *80*(6), 2032–2052.

Kim, K.-H., J.-H. Ree, Y. Kim, S. Kim, S. Y. Kang, and W. Seo (2018), Assessing whether the 2017 M_w 5.4 Pohang earthquake in South Korea was an induced event, *Science*, *360*, 1007–1009, doi:10.1126/science.aat6081.

Kortström, J., M. Uski, and K. Oinonen (2018), The Finnish National Seismic Network, *Summary of the Bulletin of the International Seismological Centre*, *52*, 41–52, doi:10.31905/59qrnanc.

Krischer, L., T. Megies, R. Barsch, M. Beyreuther, T. Lecocq, C. Caudron, and J. Wassermann (2015), ObsPy: a bridge for seismology into the scientific Python ecosystem, *Computational Science & Discovery*, *8*(1), doi:10.1088/1749-4699/8/1/014003.

Kwiatek, G., T. Saarno, T. Ader, F. Bluemle, M. Bohnhoff, M. Chendorain, G. Dresen, P. Heikkinen, I. Kukkonen, P. Leary, M. Leonhardt, P. Malin, P. Martínez-Garzón, K. Passmore, P. Passmore, S. Valenzuela, and C. Wollin (2019), Controlling fluid-induced seismicity during a 6.1-km-deep geothermal stimulation in Finland, *Science advances*, *5*, eaav7224, doi:10.1126/sciadv.aav7224.

Laloui, L., and A. F. R. Loria (2020), *Chapter 2 - Energy geostructures*, pp. 25–65, Analysis and Design of Energy Geostructures, Academic Press, doi:10.1016/B978-0-12-816223-1.00002-3.

Lamb, O. D., J. M. Lees, P. E. Malin, and T. Saarno (2021), Audible acoustics from low-magnitude fluid-induced earthquakes in Finland, *Scientific Reports*, *11*, 19206, doi:10.1038/s41598-021-98701-6.

Lecocq, T., S. P. Hicks, K. Van Noten, K. van Wijk, P. Koelemeijer, R. S. M. De Plaen, F. Massin, G. Hillers, R. E. Anthony, M.-T. Apoloner, M. Arroyo-Solórzano, J. D. Assink, P. Büyükakpınar, A. Cannata, F. Cannavo, S. Carrasco, C. Caudron, E. J. Chaves, D. G. Cornwell, D. Craig, O. F. C. den Ouden, J. Diaz, S. Donner, C. P. Evangelidis, L. Evers, B. Fauville, G. A. Fernandez, D. Giannopoulos, S. J. Gibbons, T. Girona, B. Grecu, M. Grunberg, G. Hetényi, A. Horleston, A. Inza, J. C. E.

Irving, M. Jamalreyhani, A. Kafka, M. R. Koymans, C. R. Labedz, E. Larose, N. J. Lindsey, M. McKinnon, T. Megies, M. S. Miller, W. Minarik, L. Moresi, V. H. Márquez-Ramírez, M. Möllhoff, I. M. Nesbitt, S. Niyogi, J. Ojeda, A. Oth, S. Proud, J. Pulli, L. Retailleau, A. E. Rintamäki, C. Satriano, M. K. Savage, S. Shani-Kadmiel, R. Sleeman, E. Sokos, K. Stammler, A. E. Stott, S. Subedi, M. B. Sørensen, T. Taira, M. Tapia, F. Turhan, B. van der Pluijm, M. Vanstone, J. Vergne, T. A. T. Vuorinen, T. Warren, J. Wassermann, and H. Xiao (2020), Global quieting of high-frequency seismic noise due to COVID-19 pandemic lockdown measures, *Science*, doi:10.1126/science.abd2438.

Leonhardt, M., G. Kwiatek, P. Martínez-Garzón, M. Bohnhoff, T. Saarno, P. Heikkinen, and G. Dresen (2021), Seismicity during and after stimulation of a 6.1 km deep enhanced geothermal system in Helsinki, Finland, *Solid earth*, *12*, 581–594, doi: 10.5194/se-12-581-2021.

Li, B., A.-A. Gabriel, A. Rintamäki, and G. Hillers (2021), Array based analysis of induced earthquake characteristics using beamforming and back-projection methods in Helsinki, Finland, in *EGU General Assembly 2021*, EGU21-12888, online, doi: 10.5194/egusphere-egu21-12888,2021.

Lin, T.-C., G. Hillers, S.-J. Lee, and S.-H. Hung (2020), Imaging the Internal Structure along the Longitudinal Valley Fault System, Taiwan, Using Fault Zone Head Waves, in *AGU Fall Meeting*, S062-0006, online.

Lyakhovsky, V., and E. Shalev (2021), Runaway Versus Stable Fracturing During Hydraulic Stimulation: Insights from the Damage Rheology Modeling, *Rock Mechanics and Rock Engineering*, doi:10.1007/s00603-021-02395-1.

Majer, E. L., R. Baria, M. Stark, S. Oates, J. Bommer, B. Smith, and H. Asanuma (2007), Induced seismicity associated with Enhanced Geothermal Systems, *Geothermics*, *36*, 185–222, doi:10.1016/j.geothermics.2007.03.003.

Mäntyniemi, P., K. Oinonen, P. Seipäjärvi, and T. Vuorinen (2017), Internet macroseismology in Finland: current observatory practice, in *XXVIII Geofysiikan Päivät*, edited by T. Veikkolainen, L. Tuomi, T. Korja, I. Suomi, M. Nordman, M. Bilker-Koivula, and S. Väkevä, pp. 44–48, Geosfysiikan Seura (Geophysical Society of Finland).

Martínez-Garzón, P., G. Kwiatek, M. Bohnhoff, and G. Dresen (2017), Volumetric components in the earthquake source related to fluid injection and stress state, *Geophysical Research Letters*, *44*, 800–809, doi:10.1002/2016GL071963.

McGarr, A. (2014), Maximum magnitude earthquakes induced by fluid injection, *Journal of Geophysical Research: Solid Earth*, *119*, 1008–1019, doi:10.1002/2013JB010597.

Pajunen, M., M.-L. Airo, T. Elminen, R. Niemelä, J. Salmelainen, M. Vaarma, P. Wasenius, and M. Wennerström (2008), Construction suitability of bedrock in the Helsinki area based on the tectonic structure of the Svecofennian crust of southern Finland, *Geological Survey of Finland, Special Paper*, *47*, 309–326.

Renard, F., J. McBeck, N. Kandula, B. Cordonnier, P. Meakin, and Y. Ben-Zion (2019), Volumetric and shear processes in crystalline rock approaching faulting, *Proceedings of the National Academy of Sciences of the United States of America*, *116*, 16,234–16,239, doi:10.1073/pnas.1902994116.

Schmittbuhl, J., O. Lengline, S. Lambotte, M. Grunberg, C. Doubre, J. Vergne, F. Cornet, and F. Masson (2021), Induced and triggered seismicity from Nov 2019 to Dec 2020 below the city of Strasbourg, France, in *EGU General Assembly 2021*, EGU21-8374, online, doi:10.5194/egusphere-egu21-8374.

Shalev, E., and V. Lyakhovsky (2018), The role of the intermediate principal stress on the direction of damage zone during hydraulic stimulation, *International Journal of Rock Mechanics and Mining Sciences*, *107*, 86–93, doi:10.1016/j.ijrmms.2018.05.001.

Shalev, E., M. Calò, and V. Lyakhovsky (2013), Formation of damage zone and seismic velocity variations during hydraulic stimulation: numerical modelling and field observations, *Geophysical Journal International*, *195*, 1023–1033, doi:10.1093/gji/ggt279.

Snoke, J. A. (2003), FOCMEC: FOCal MEChanism Determinations, in *International Handbook of Earthquake and Engineering Seismology, Part B*, edited by W. H. Lee, H. Kanamori, P. C. Jennings, and C. Kisslinger, pp. 1629–1630, Academic Press, United Kingdom, doi:10.1016/S0074-6142(03)80291-7.

Taylor, G., G. Hillers, and T. A. T. Vuorinen (2021), Using array-derived rotational motion to obtain local wave propagation properties from earthquakes induced by the 2018 geothermal stimulation in Finland, *Geophysical Research Letters*, doi: 10.1029/2020GL090403.

Terakawa, T., S. A. Miller, and N. Deichmann (2012), High fluid pressure and triggered earthquakes in the enhanced geothermal system in Basel, Switzerland, *Journal of Geophysical Research: Solid Earth*, *117*, B07305, doi:10.1029/2011JB008980.

Tiira, T., T. Janik, T. Skrzynik, K. Komminaho, A. Heinonen, T. Veikkolainen, S. Väkevä, and A. Korja (2020), Full-Scale Interpretation of Kokkola-Kymi (KOKKY) Seismic

Profile, Fennoscandian Shield, *Pure and Applied Geophysics*, *177*, 3775–3795, doi: 10.1007/s00024-020-02459-3.

Uski, M., and A. Tuppurainen (1996), A new local magnitude scale for the Finnish seismic network, *Tectonophysics*, *261*, 23–37, doi:10.1016/0040-1951(96)00054-6.

van der Elst, N. J., M. T. Page, D. A. Weiser, T. H. W. Goebel, and S. M. Hosseini (2016), Induced earthquake magnitudes are as large as (statistically) expected, *Journal of Geophysical Research: Solid Earth*, *121*, 4575–4590, doi:10.1002/2016JB012818.

Vasterling, M., U. Wegler, J. Becker, A. Brüstle, and M. Bischoff (2017), Real-time envelope cross-correlation detector: application to induced seismicity in the Insheim and Landau deep geothermal reservoirs, *Journal of Seismology*, *21*, 193–208, doi: 10.1007/s10950-016-9597-1.

Veikkolainen, T., M. Uski, A. I. Voutilainen, T. Vuorinen, K. Oinonen, J. Kortström, T. Luhta, P. Mäntyniemi, and T. Tiira (2020), Seismisyys Espoon Otaniemen syväreikähankkeen viimeistelyvaiheessa, *Tech. Rep. T-102*, Institute of Seismology, University of Helsinki.

Veikkolainen, T., J. Kortström, T. Vuorinen, I. Salmenperä, T. Luhta, P. Mäntyniemi, G. Hillers, and T. Tiira (2021a), The Finnish National Seismic Network: Toward Fully Automated Analysis of Low-Magnitude Seismic Events, *Seismological Research Letters*, *90*, 1581–1591, doi:10.1785/0220200352.

Veikkolainen, T., K. Oinonen, T. Vuorinen, J. Kortström, P. Mäntyniemi, P. Lindblom, M. Uski, and T. Tiira (2021b), Helsingin seisminen asemaverkko ja seismisyys 2020, *Tech. Rep. T-103*, Institute of Seismology, University of Helsinki.

Voutilainen, A. (2021), A New Ground Motion Prediction Equation for Otaniemi, Espoo, South-Finland, MSc Thesis, University of Helsinki, http://urn.fi/URN:NBN:fi:hulib-202105242333.

Wegler, U., T. Eulenfeld, T. A. T. Vuorinen, and G. Hillers (2020), Attenuation properties and source spectra from earthquakes induced by the 2018 geothermal reservoir stimulation in Espoo/Helsinki, southern Finland, in *AGU Fall Meeting*, S010-0011, online.

Wessel, P., W. H. F. Smith, R. Scharroo, J. Luis, and F. Wobbe (2013), Generic Mapping Tools: Improved Version Released, *EOS Transactions AGU*, *94*, 409–410, doi: 10.1002/2013EO450001.

Annukka E. Rintamäki
Gregor Hillers
Tommi A. T. Vuorinen
Tuija Luhta
Jonathan M. Pownall
Christina Tsarsitalidou
Jukka Keskinen
Jari T. Kortström
Tzu-Chi Lin
Kati J. Oinonen
Tahvo J. Oksanen
Päivi B. Mäntyniemi
Pirita J. Seipäjärvi
Marja R. Uski
David M. Whipp
PO BOX 68 (Pietari Kalmin katu 5)
FI-00014 University of Helsinki
Finland

Keith Galvin
Terravision Exploration
401 Walton Road
Molesey
Surrey
United Kingdom
KT8 2EG

George Taylor
Ocean Environment Team
United Kingdom Hydrographic Office
Taunton
United Kingdom
TA1 2DN

Ahti I. Voutilainen

Boliden Minerals AB
Finnforsvägen 4
93632 Boliden
Sweden

Table 1. Subnetworks, instrumentation, and acquisition parameters of the 2019−2020 Helsinki area deployment. Acronyms: ED = Earth Data PS6-24, Centaur = Nanometrics Centaur. A '?' in the Station code column is a regular expression pattern.

Subnet-work code	Station group	Permanent/ Temporary	Online	Station code	Receiver	Recorder	Sampling rate (Hz)	Gain (dB)	N:o stations	Owner
HE	FNSN	permanent	yes	MEF NUR PVF	Trillium 120P GS13 Trillium Compact	ED ED Centaur	100-250		3	ISUH
	HEL	semipermanent	yes	HEL1–HEL5	Trillium Compact	Centaur	250		5	ISUH
	HelsinkiNet	permanent	yes	KUNI LAUT VUOS	Trillium Compact	Centaur	250		3	ISUH
OT	Cube	temporary	no	???50 for single stations or ??50, ??51 etc. for array stations	3-D Geophone PE-6/B 4.5 Hz	DATA-CUBE3	400	16	70	GIPP
OX	SmartSolo	temporary	no		IGU-16HR 3C 5Hz	Integrated Smart-Solo recorder	500	18	43	ISUH
	REF TEK	temporary	no		Lennartz LE-3Dlite 1Hz	REF TEK 130-01	500	32	3	ISUH

Table 2. Short-period array and station deployment details.

Array or station	Location name	Lat [°]	Lon [°]	Station type	Number of stations	Operation started	Operation ended
AS	Lauttasaari	60.163	24.891	SmartSolo	6	7 May 2020	8 Jun 2020
EV	Elfvik	60.204	24.821	Cube	11	19 Dec 2019	14 Jul 2020
KS	Koirasaari	60.085	24.847	Cube, SmartSolo	3, 4	30 Mar 2020	10 Jun 2020
MN	Munkkiniemi	60.201	24.869	SmartSolo	16	6 May 2020	22 May 2020
SH	Storhemt	60.193	24.735	SmartSolo	17	6 May 2020	22 May 2020
SS	Seurasaari	60.184	24.883	Cube	7	29 Nov 2019	13 Jul 2020
TL	Toppelund	60.158	24.783	Cube	7	13 Dec 2019	14 Jul 2020
EK	Espoon keskuspuisto	60.185	24.714	Cube	4	20 Dec 2019	14 Jul 2020
IL	Ilola	60.331	25.034	Cube	3	8 Apr 2020	14 Jul 2020
KL	Klaukkala	60.388	24.756	Cube	3	4 Mar 2020	14 Jul 2020
LK	Latokartano	60.225	25.049	Cube	3	3 Dec 2019	13 Jul 2020
LR	Lähderanta	60.244	24.741	Cube	3	5 Mar 2020	14 Jul 2020
LS	Laajasalo	60.171	25.065	Cube	3	25 Feb 2020	13 Jul 2020
PH	Paloheinä	60.259	24.896	Cube	3	3 Dec 2019	13 Jul 2020
PK	Poliisien kesäkoti	60.152	24.858	Cube	4	5 Mar 2020	14 Jul 2020
PM	Pajamäki	60.221	24.856	Cube	4	11 Dec 2019	13 Jul 2020
PO	Porkkala	60.091	24.505	Cube	3	10 Dec 2019	14 Jul 2020
SL	Suomenlinna	60.144	24.993	Cube	3	28 Nov 2019	1 Jul 2020
SV	Solvalla	60.295	24.558	Cube	3	10 Dec 2019	14 Jul 2020
DID50	Didrichsen art museum	60.186	24.856	Cube	1	29 Nov 2019	13 Jul 2020
HAN50	Hanaholmen Cultural Centre	60.164	24.835	Reftek	1	23 Apr 2020	29 May 2020
KAL50	Hotel Kalastajatorppa	60.191	24.874	Cube	1	18 Dec 2019	13 Jul 2020
PIR50	Pirkkola	60.232	24.908	Cube	1	1 Apr 2020	13 Jul 2020
WEG50	Exhibition Centre Weegee	60.180	24.794	Reftek	1	17 Apr 2020	15 Jun 2020
ZAK50	Gallen-Kallela Museum	60.206	24.839	Reftek	1	23 Apr 2020	15 Jun 2020

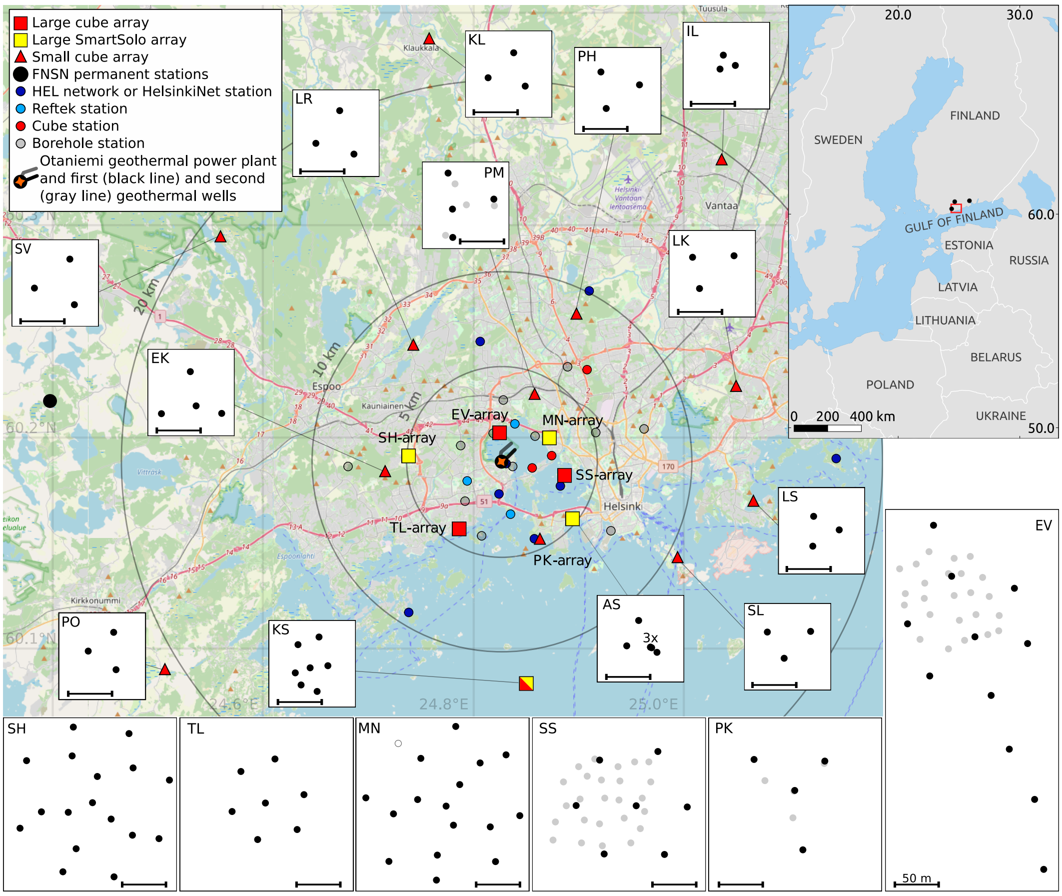

Figure 1. The 2020 network in the Helsinki capital area, around the Otaniemi EGS stimulation site indicated by the red star in the center of the map (one borehole station and one HEL network station are hidden under the site symbol). Symbols are explained in the upper left legend. The red rectangle in the upper right index map shows the location of the study area in southern Finland. Black circles in the index map are FNSN stations. The configurations of the 19 arrays consisting of 3 to 17 stations are shown in the insets that are all on the same scale. For array abbreviations see Table 1. In these insets the 2020 temporary stations are shown as black dots, and gray dots indicate the 2018 sensor locations. The open symbol in the MN array inset indicates the lost sensor. Base map and data from OpenStreetMap and OpenStreetMap Foundation.

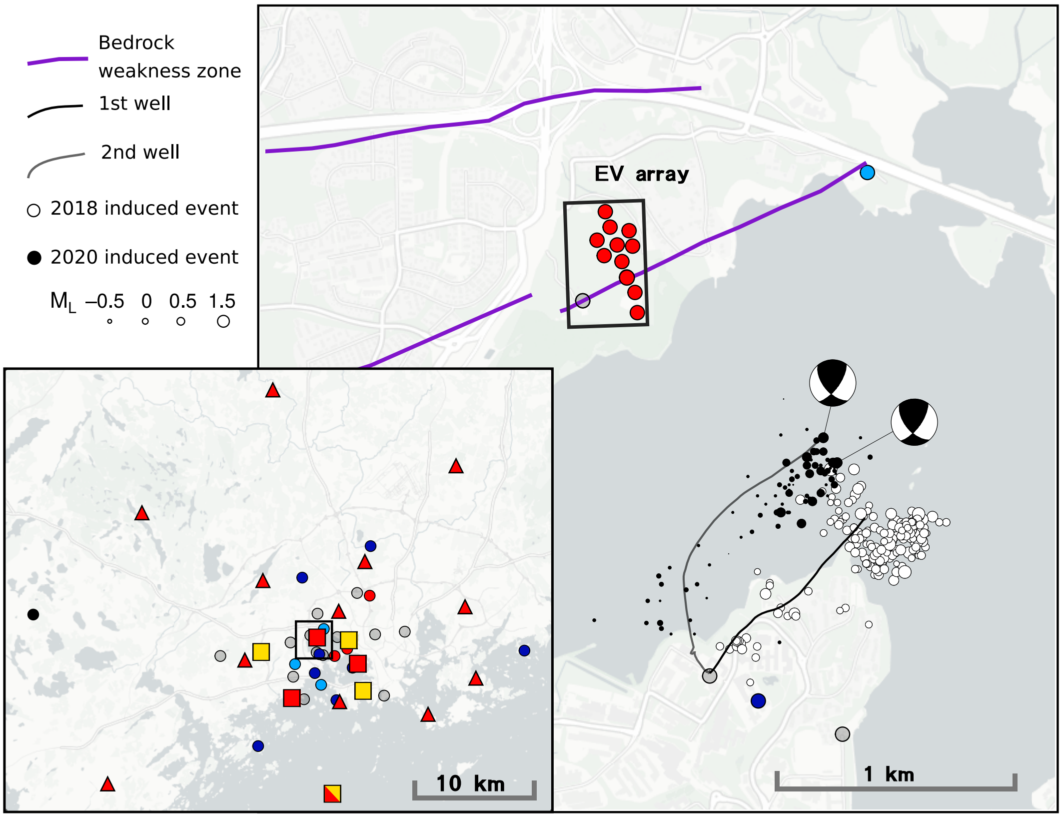

Figure 2. Close-up of the stimulation area. The location of the map to the right is indicated by the black rectangle in the lower left index map that covers the same area as Figure 1. Station and array symbols are as in Figure 1. The 203 largest seismic events induced in 2018 [*Hillers et al.*, 2020] and 83 automatically detected induced events in 2020 are shown. The two beachballs indicate the source mechanisms of two 2020 M_{L}1.2 events. Bedrock weakness zones are discussed in Chapter Geological structures at Elfvik. The well-head on the Fortum district heating site is located at the Aalto University campus in Otaniemi, Espoo. Base map and data from OpenStreetMap, OpenStreetMap Foundation and CARTO.

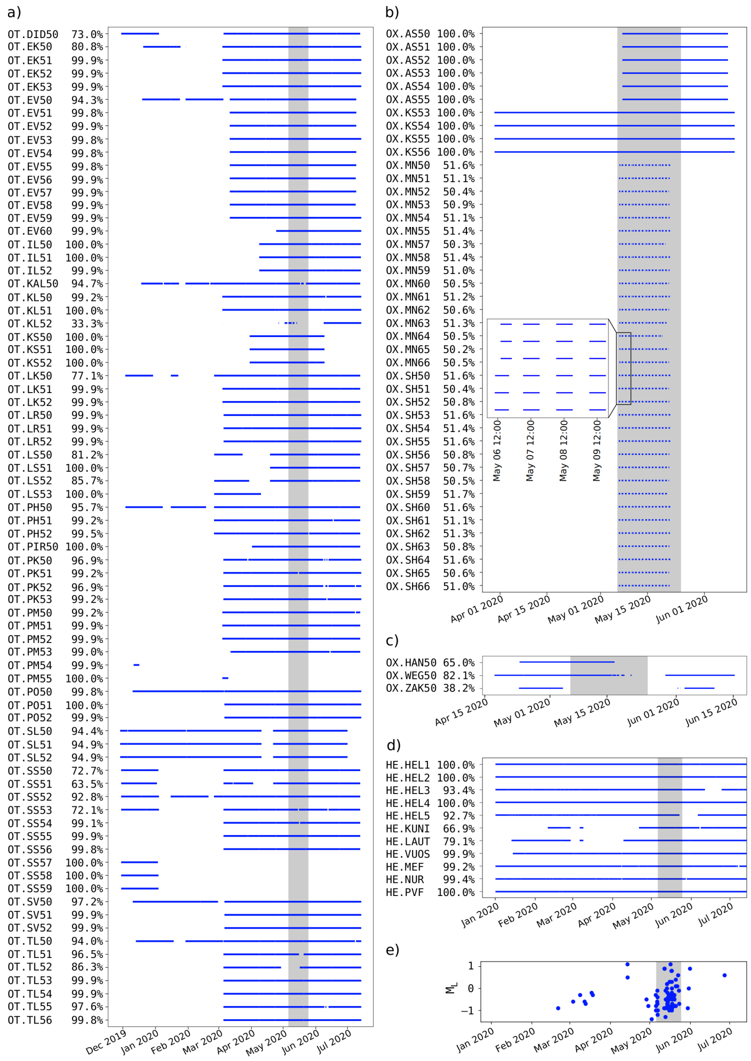

Figure 3. Data availability plots. The gray indicated interval shows the duration of the stimulation from 6 May 2020 to 24 May 2020. (a) The OT cube subnetwork. Some stations were deployed in November and December 2019, but the majority of the stations started to record early March 2020. Data gaps can be both intentional or unintentional (see Chapter Temporary stations). (b) SmartSolo stations of the OX subnetwork. Data collected with SmartSolos using external batteries is continuous. Data collected with SmartSolos powered by internal batteries have 12-hour on-off intervals. (c) Reftek stations of the OX subnetwork. The Refteks did not record for the whole duration of the stimulation due to a shorter-than-expected battery life. The COVID-19 related restrictions led to maintenance intervals that were longer than necessary. (d) HE subnetwork. The HelsinkiNet stations VUOS, LAUT, KUNI were installed in 2020 before the stimulation. LAUT and KUNI were tested between January and March before being permanently installed in April 2020. (e) The timeline of induced events.

Figure 4. Installation impressions. (a,b) The air-alkaline batteries were prepared in a water-proof, compact, and inexpensive packaging with sufficient air-flow. The batteries were wrapped in plastic bags with a hose attached close to the air-holes at the top of the battery. (c) A typical installation site in the suburban Helsinki capital area. Most stations were installed on bedrock outcrops in a decimeters-thick organic soil or peat layer. (d) We used sand for better coupling of the geophones. (e) The batteries and recorders were placed in a shallow hole and camouflaged. Photographs by A. Rintamäki.

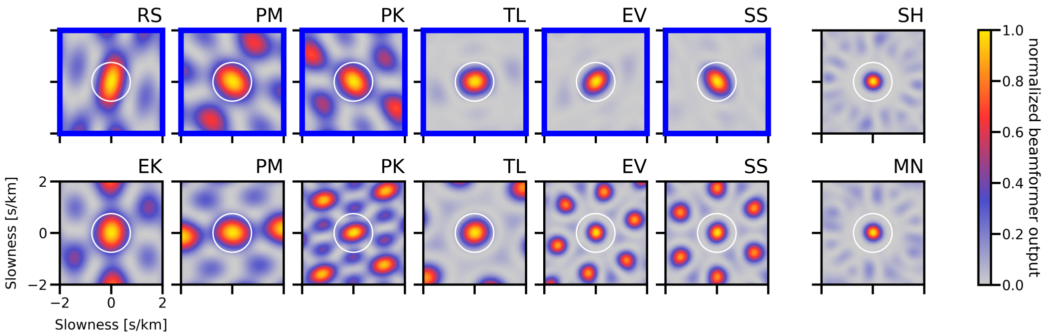

Figure 5. Array response functions for a 10 Hz plane wave. The left six arrays were deployed in 2018 (upper panel) and 2020 (lower panel) at the same or corresponding sites. The white circle at a slowness of 0.75 s/km facilitates the comparison with the beamforming results in *Hillers et al.* [2020]. Clean functions corresponding to the 2018 TL, EV, and SS arrays and to the 2020 SH and MN arrays reflect the relatively large number of stations.

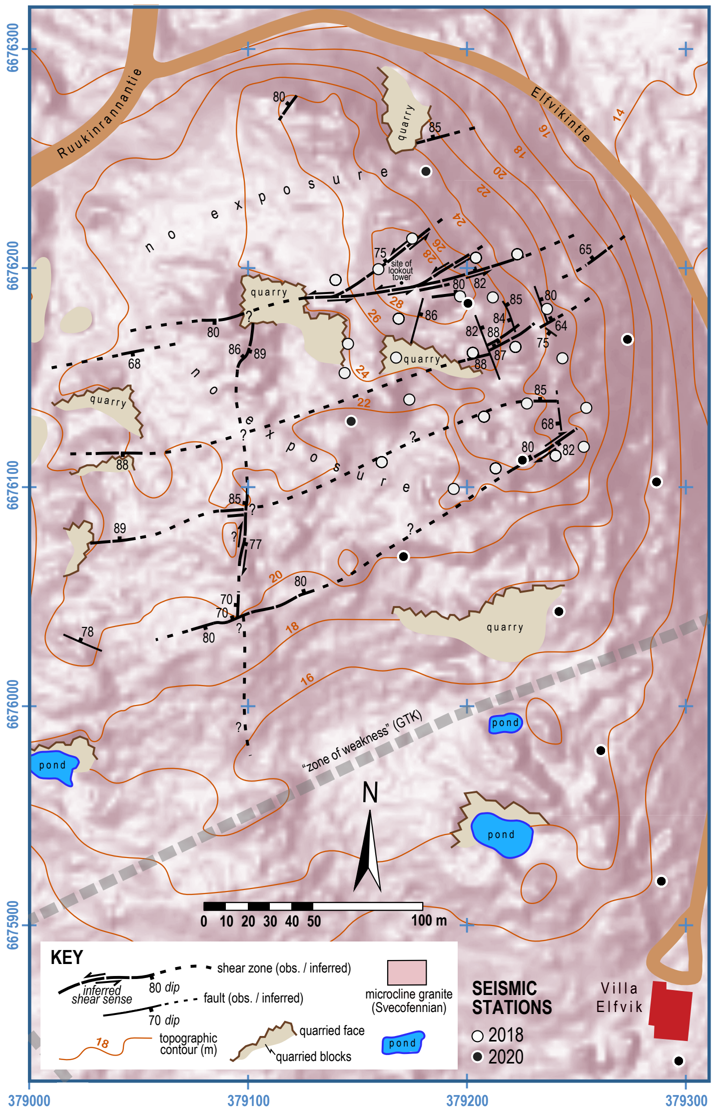

Figure 6. Geological map of surface expressions of shear zone structures at the Elfvik site 2 km to the north-west of the borehole. The area is indicated by the EV array rectangle in Figure 2, it covers ∼0.13 km^2. The 2018 and 2020 array station locations are shown by white and black circles, respectively. The gray dashed "zone of weakness" corresponds to the purple line in Figure 2 that intersects the EV array. GTK refers to *Pajunen et al.* [2008]. Lithology data from the Geological Survey of Finland and Lidar elevation model from the National Land Survey of Finland.

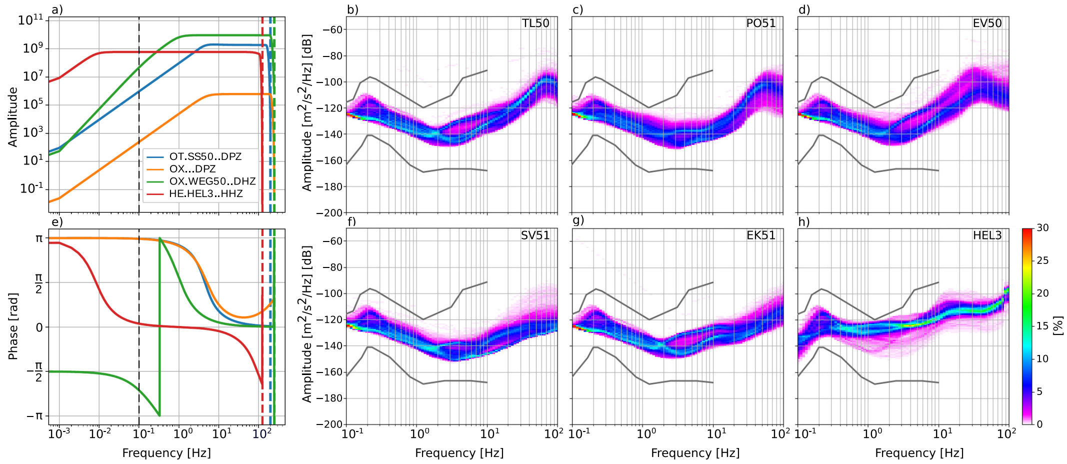

Figure 7. (a,e) Instrument responses of the three types of temporary sensors and a broadband sensor of the HEL network. (b–d, f–h) Probabilistic power spectral density (PPSD) plots of selected stations from urban (b,d,h), coastal (b,d), or remote (c,f,g) locations. (b–d, f, g) PPSD plots of cube stations with 4.5 Hz geophones converge to a narrow band at 0.1 Hz due to limited low-frequency resolution. We attribute the prominent peak at 60 to 70 Hz to anthropogenic activity and low attenuation.

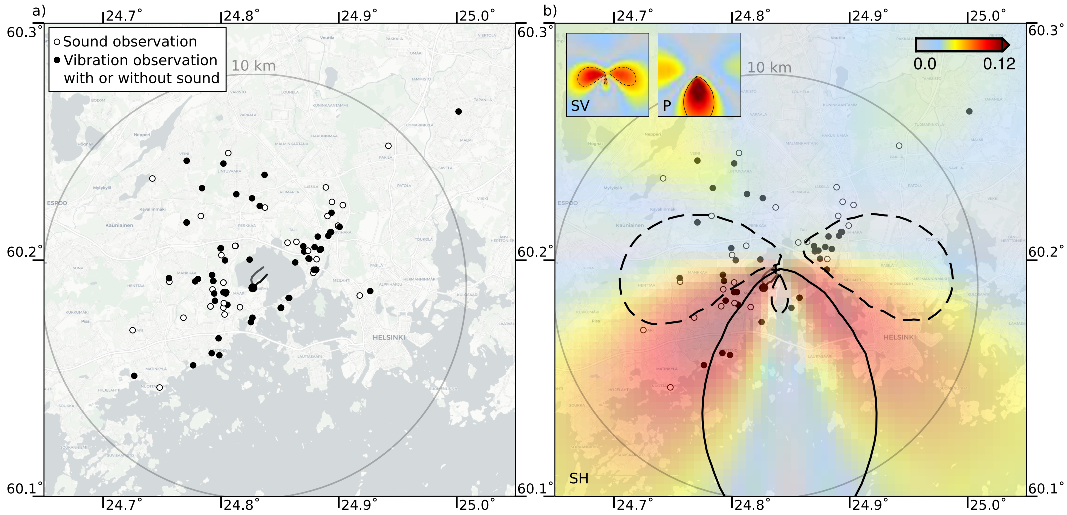

Figure 8. Macroseismicity and radiation patterns. (a) All macroseismic observations associated with the 2020 EGS stimulation. (b) Macroseismic observations of the two largest induced M_{L}1.2 events and the SH radiation pattern that is practically identical for the two events (cf the source mechanisms in Fig. 2). SV and P radiation patterns are shown in the insets, and the associated contours are also shown in the main figure. Geometrical spreading is accounted for.

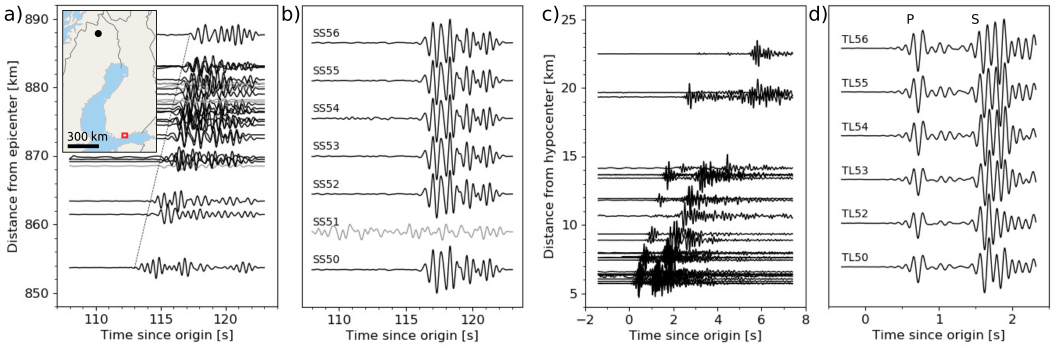

Figure 9. Vertical component velocity waveform data recorded by the short period cube and SmartSolo stations. The instrument response has not been deconvolved. (a) P wave seismograms in the 0.5−2.5 Hz frequency range from the 18 May 2020 $M_{\mathrm{w}}4.1$ Kiruna mine collapse event in Sweden. The dashed line indicates a propagation speed of 8 km/s. Data with low signal-to-noise ratio are plotted in gray. The locations of the epicentre (black circle) and the network (red rectangle) are illustrated in the inset. (b) Kiruna mine event P wave records from the SS array. (c) Seismograms of a 5.6 km deep induced $M_{\mathrm{L}}1.2$ event in the 1−10 Hz range. (d) P wave and S wave arrivals recorded at the TL array. The hypocentral distance is 7.7 km.

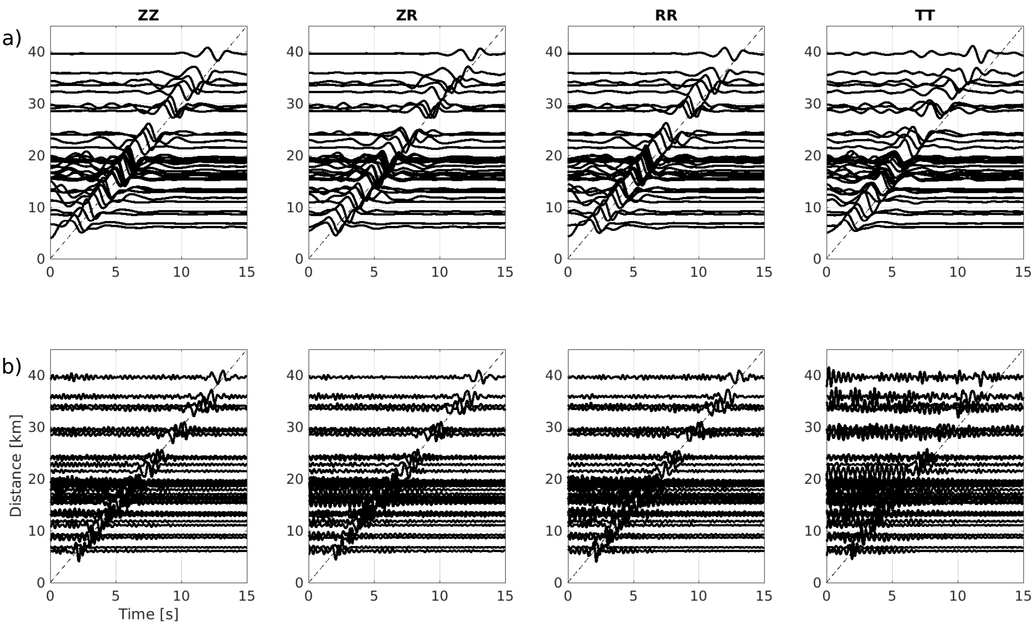

Figure 10. Ambient noise cross-correlation functions obtained from cube station array data. The 0.25−1 Hz range (a) and 1−4 Hz range (b) results show clear signals of propagating Rayleigh and Love waves. The dashed lines indicate a propagation speed of 3 km/s.